

Flow Regime and Reynolds Number Variation Effects on the Mixing Behavior of Parallel Flows¹

Abdullah G. Weiss^a, Paul Kristo^b, Juan R. Gonzalez^a, Mark L. Kimber^{a,b,2}

^aDepartment of Nuclear Engineering, Texas A&M University, College Station, TX, 77843

^bDepartment of Mechanical Engineering, Texas A&M University, College Station, TX, 77843

¹ Revised draft submitted to Experimental Thermal and Fluid Science on December 16, 2021.
Corresponding author mark.kimber@tamu.edu

Abstract

The hydraulic single-phase mixing of three parallel rectangular channels is experimentally investigated at various Reynolds numbers (Re) and flow regime combinations. Particle Image Velocimetry results for seven mixing cases are presented and discussed with varying Re combinations ranging from 1,824-20,844. While all cases result in the same Re ratio of ~ 0.69 between the inner and outer flows, two cases represent multi-regime mixing with the inner-outer regime pair of laminar-transitional and transitional-turbulent, while the other 5 cases are all characteristic of turbulent mixing with varying levels of turbulence. The outer channels initially share characteristics with a backward facing step. The center channel is found to initially behave like a slot jet, but then sees a significant increase in velocity decay. This inner flow velocity decay increased dramatically in the laminar-transitional mixing case, whose centerline velocity decay was ~ 6 times larger than the decay in the turbulent mixing cases. Second order statistics revealed a consistent mixing layer thickness of ~ 0.1 hydraulic diameters for all the cases but showed more intense shearing in the multi-regime mixing cases. The combined point and thereby the mixing layer length is determined using centerline velocity decay profiles, which show a much more aggressive mixing in multi-regime flows. Multi-regime mixing demonstrated superior characteristics relative to turbulent mixing due to a more dramatic velocity decay in the inner flow and a shorter mixing length. **The contributions of this work include communicating the benefits of multi-regime mixing and providing detailed characterization efforts that can serve future efforts for validating computational models.** This research **also** lays the groundwork for future studies aimed at achieving high levels of mixing without a severe penalty in pressure drop.

Keywords

Mixing; Flow Regime; PIV; Mixing Layers; Shear Layers; Turbulence

1. Introduction

The hydraulic behavior of mixing flows can generally be characterized by the momentum and energy transfer between the flows under different conditions ranging from geometrical constraints to inlet flow characteristics. This behavior can be assessed experimentally by performing velocimetry measurements that characterize the spatio-temporal evolution of the flow field. Mixing experiments typically consist of separated fluid streams of varied characteristics exiting nozzles of a particular geometries and entering a shared volume whose geometry can have significant effects on the mixing characteristics. Such shared volume consists of either a relatively open volume or a confined one per Figure 1 (a) and (b), respectively.

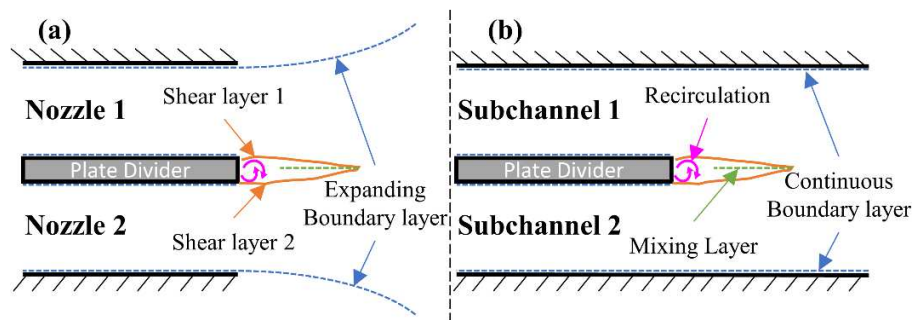


Figure 1. Schematics of mixing in (a) an open shared volume and (b) a confined shared volume. The expected flow behavior in both cases is illustrated and labeled. It should be noted that this work more closely resembles the confined mixing configuration presented in (b).

When streams of separated flows coalesce on an open volume as shown in Figure 1 (a), the boundary layers are physically shifted in space, expanding as the flows progress further downstream due to the opening in the fluid domain. This opening promotes adverse pressure gradients that lead to the expansion in the mixed flow. On the other hand, the scenario where flows coalesce on a confined volume such as the shown in Figure 1 (b), the boundary layer does not expand due to the fixed bounds of the fluid domain. Contrary to the open mixing scenario in Figure 1 (a), the confined mixing scenario nominally promotes a zero-pressure gradient (at least in the initial mixing region) [1], maintaining the continuous boundary

layer. It should be noted that although the boundary layer does not expand (shift spatially) in confined mixing, its thickness is expected to grow as the flows continue mixing.

Even though the geometry of the shared volume affects the mixing evolution, primarily due to changes in the boundary layer, there are many shared characteristics between the two flows that can enable direct comparisons. For starters, the presence of a plate or divider separating the two flows prior to mixing is expected to induce recirculation zones or pockets regardless of the shared volume geometry. Additionally, per Figure 1, the presence of two shear layers and one mixing layer when two streams are mixing is also expected regardless of the shared volume geometry. Each shear layer corresponds to its respective fluid stream experiencing shearing as it expands towards the neighboring fluid stream. The mixing layer is naturally representative of the two streams coalescing towards each other, thereby mixing. Finally, the recirculation pocket is due to the flows attempting to overcome the shear layers and converge upon each other. As such, the length of the recirculation pocket is synonymous with the reattachment length. Those features are expected regardless of the shared volume geometry, and they are the primary subject of this work.

Experimentally, confined channel flow experiments provide more control over the flow in the sense that the outer boundary layer behavior, difficult as it may be to characterize experimentally, is not as complex as it would be in jet experiments where the expansion of the flow area is inevitable. On the other hand, jet experiments yield high velocity fluctuations relative to local mean velocities, especially near the edges of the plume. In many instances, the fluctuations can exceed 40% of the mean velocity magnitude, even at low Reynolds numbers [2]. This can lead to confusion when interpreting measurements as greater inlet turbulence intensities can contribute to bigger uncertainties when looking at higher order turbulence statistics downstream from the inlet [3], and presumably in the mixing region as well. This makes confined channel flows a suitable candidate for better understanding the fundamental fluid behavior between mixing flows.

Of interest to this paper are the effects of Reynolds number variations to the mixing behavior between three parallel flows from rectangular channels. Several jet mixing experiments can be found in literature studying the effects on different turbulence parameters due to alterations in the inlet nozzle geometry [4], spacing [5, 6], orientation [7, 8], and velocity ratios between different jets [9, 10, 11]. Although alterations in nozzle geometry and/or velocity may be considered as an alteration in the Reynolds number, it is difficult to find literature that provides an exclusive look at how Reynolds number variations between the channels affect the mixing behavior and corresponding turbulence statistics regardless of velocity ratios. From a fundamental point of view, investigating quasi-iso-velocity mixing with flow regime variations between channel flows can provide a clear understanding of the mixing behavior as a function of Reynolds number variations exclusively.

One of the applications where such multi-regime mixing is relevant is **the** mixing in blood streams during drug infusions, saline injections, and blood transfusions, especially in view of the mixing effects on endothelial shear stresses [12, 13]. A better understanding of multi-regime mixing would also allow for a deeper discussion on the importance of single-phase flow regimes when considering mixing for a variety of applications. This is particularly relevant when considering the aforementioned medical applications, but also for off-nominal and emergency cooling operation in nuclear reactors [14] as well as the design of fuel assembly spacer grids in said reactors [15].

The multi-regime mixing studies in this paper seek to provide a much-needed elaboration on the fundamental effects of flow regimes on the mixing phenomenon, as no literature considers flow regimes as an actual factor of how mixing profiles develop, preferring to stick to nozzle size/geometry and inlet velocity as the primary indications of how mixing flows develop. Such investigations would require a facility capable of replicating laminar and turbulent flows alike in separate channels, meaning that it would also be capable of reproducing transition flows under certain conditions. The matched index of refraction (MIR) tunnel in the Thermal Hydraulics Verification and Validation (THVV) Laboratory at Texas A&M University provides these multi-regime mixing capabilities. Originally designed to study

flows around complex geometries and produce high quality validation metrics to aid in computational efforts [16, 17], the THVV MIR tunnel allows for optically accessible measurements of multi-regime flows in rectangular channels and is capable of matching the working fluid's refractive index to any solid quartz model. This allows for complete optical accessibility to any flow around complex geometry such as the lower plenum of a high-temperature gas reactor [18]. The design of the tunnel as well as its characterizations will be discussed prior to discussing any particle image velocimetry (PIV) multi-regime mixing results, providing the reader with a full perspective of the experimental setup and the inlet flow behavior. The multi-regime mixing is achieved via a special test section outfitted with walls to create two identical sub-channels surrounding an inner sub-channel that is relatively thinner. The walls begin and end abruptly, meaning that recirculation zones or pockets are expected. As such, the resulting mixing phenomenon of interest to this paper combines aspects of jet and confined channel mixing, as well as a backwards facing step in the case of the outer sub-channels.

This paper describes the design of the THVV MIR tunnel as well as the PIV data acquisition setup for the mixing experiments in detail and showcases the results of thorough inlet flow characterization. The characterization studies investigate the bulk flow's thermal characteristics and provides detailed accounting of the velocity, turbulence intensity, and flow angularity of the inlet flow. The characterization efforts also include uncertainty quantification of the obtained metrics and demonstrate the statistical convergence of the inlet flow velocimetric data. The results show data from seven mixing experiments with varying Reynolds number combinations but identical Reynolds number ratios, two of which yield multi-regime mixing. The resulting 1st order, 2nd order, and velocity decay behaviors are investigated with discussions of the unique physical features in this flow scenario and the effects of varying flow regimes. This work addresses gaps in literature regarding the fundamental effects of flow regimes on the mixing phenomenon, and experimentally compares the mixing characteristics of multi-regime and turbulent mixing. This paper also provides detailed characterization metrics that can be valuable in future CFD validation efforts investigating transition between laminarity and turbulence.

2. Experimental Setup

2.1 Flow Facility Description

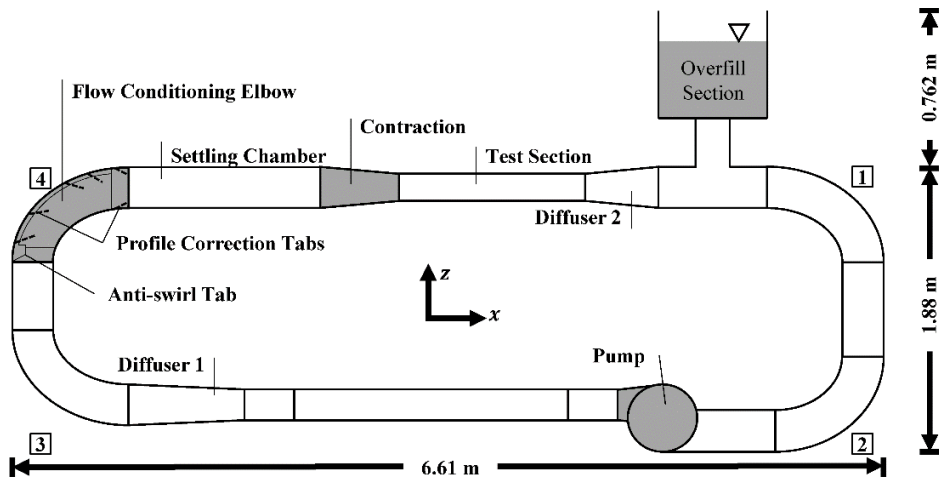


Figure 2. The THVV MIR tunnel schematic, where the flow is motivated in the counter-clockwise direction.

The THVV MIR tunnel displayed in Figure 2 is a low speed, closed-loop facility that circulates $\sim 0.5 \text{ m}^3$ of Drakeol[®] 5 light mineral oil. The tunnel is capable of speeds in the range of 1.08 to 8.19 m/s corresponding to Reynolds numbers in the range of 5603 to 43,000 coming out of the contraction leading up to the test section. The overall dimensions of the facility consist of a floor footprint of 6.61 m by 2.64 m and a height of 1.88 m (excluding the overfill section, which when included yields a maximum height of 2.64 m). The flow is motivated in the counter-clockwise direction by an Armstrong 4300 vertical in-line centrifugal pump coupled with a 20 hp, 3 phase variable frequency drive. The drive is capable of flow control within $\pm 0.001 \text{ Hz}$ and typical operating frequencies are in the range of 6 Hz to 40 Hz for this tunnel. Excluding the test section and pump, the entirety of the primary loop consists of stainless-steel piping and three fiberglass components (two diffusers and one contraction). In reference to Figure 2, the flow starts from the pump and travels towards the first diffuser that connects the 15.24 cm diameter piping with the 25.4 cm diameter piping. The flow then issues upwards and is routed through a Vortab ElbowTM Model: 10.S1-2-5-0-1 flow conditioning elbow at corner 4. The internally finned elbow includes an anti-swirl tab along the outer bend of the elbow alongside four profile correction tabs, all of which

generate vortices that counteract the existing swirls in the flow. An additional four symmetrically arranged profile correction tabs are also present at the outlet to further homogenize the velocity profile without swirls. The outlet from the elbow leads to the settling chamber, which consists of a 0.254 m diameter stainless steel pipe that is 0.965 m in length or 3.8 hydraulic diameters, per the recommendations given by the flow conditioner manufacturer.

The flow then passes through a contraction with a fifth order polynomial profile and a length to diameter ratio of 1.5, designed in accordance with the recommendations provided by Bell [19]. The contraction ratio of 1.5 yields variations between the maximum and centerline outlet velocity that are ~1% as proven by Nedyalkov [20], providing a close-to-fully developed profile [21]. Typical water tunnel designs have contraction area ratios between 6 and 9; therefore, the contraction utilized in this MIR tunnel with an area ratio of 7.9 is consistent with existing solutions. The contraction is a key component in managing turbulence at the inlet of the test section. Its design reduces the turbulence intensity and provides a flat or uniform velocity profile at the test section inlet [19-21]. Assessment of this profile will be discussed later in this study.

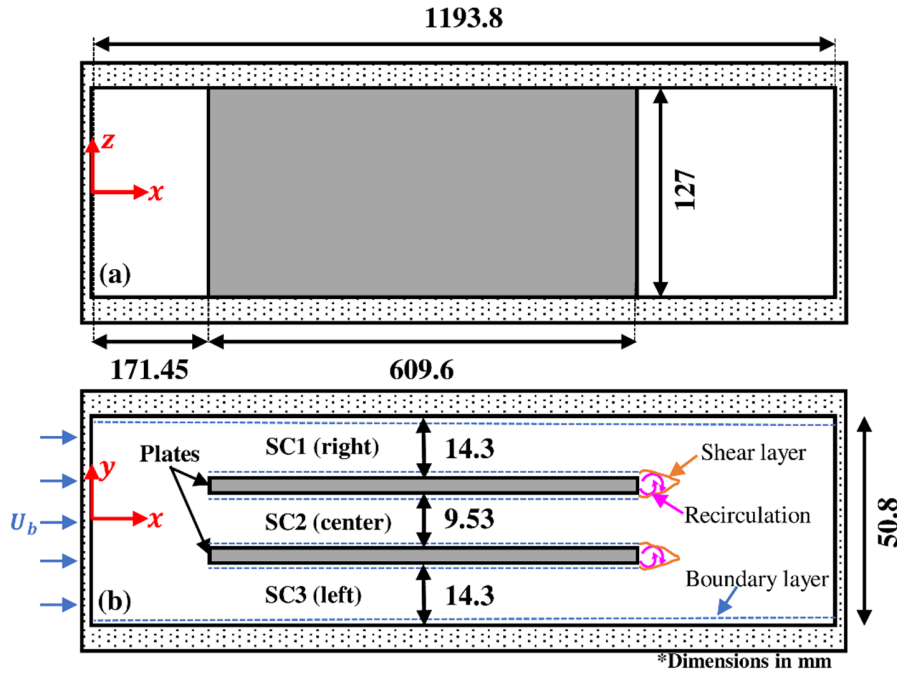


Figure 3. The first subsection of the rectangular test section, with the quartz plates acting as sub-channel walls for the separated flows. The side view shown in (a), while the bottom view is shown in (b) with the expected flow behavior. All dimensions are in mm.

The rectangular test section is composed of two identical acrylic sub-sections providing an optically accessible region that is 2387.6 mm \times 50.8 mm \times 127 mm in the streamwise x , spanwise y , and transverse z directions, respectively. The side test section walls (along the y -direction) are 12.7 mm thick with a tolerance of ± 0.127 mm while the top and bottom test section walls (along the z -direction) are 25.4 mm thick with a tolerance of ± 1 mm. Of interest to this paper is the first subsection, whose side view, corresponding to the transverse xz -plane, is shown in Figure 3 (a) while Figure 3 (b) shows the bottom view, corresponding to the spanwise xy -plane. Rectangular grooves 6.35 mm wide (± 0.127 mm) and 12.7 mm deep (± 1 mm) are machined in the top and bottom walls of the first subsection to house the current geometry. This geometry consists of two 609.6 mm \times 6.35 mm \times 152.4 mm quartz walls, fitted into the grooves for mixing studies. The quartz plates are placed 152.4 mm downstream of the test section inlet and span the height of the test section (z -direction). As seen in Figure 3 (b), the plate spacing is 9.53 mm forming the center or inner sub-channel (SC2), where the outer sub-channels (SC1 is right, and SC3

is left) are made up from the balance of the test section width and are each 14.3 mm wide. These three sub-channels enable laminar, transition, and turbulent mixing as determined by the pump control setting. The dimensions of the main channel are used to calculate a hydraulic diameter ($D = 72.57$ mm), which will be used to normalize the dimensions in the mixing experiment. This main channel extends to the second sub-section, which spans another 1193.8 mm to complete the rest of the test section length. The second sub-section serves as a tool to investigate the flow development further downstream. Although it is not utilized in any of the experiments presented in this paper, its availability is beneficial for future studies where additional downstream hydraulic diameters could be needed for a flow to develop further. It should be noted that the hydraulic diameter is calculated with the main channel dimensions as opposed to the dimensions of any of the sub-channels. This is a notable distinction when it comes to mixing results comparisons, as many confined and free flow mixing studies tend to use the nozzle dimensions to normalize their data (the sub-channel dimensions in this case) [4-11]. As such, what could be interpreted as 10 hydraulic diameters in this study would correspond to 30+ hydraulic diameters in other studies. For the reader's convenience, the hydraulic diameter of the inner sub-channel (SC2) is found to be 17.73 mm while the hydraulic diameter for each of the outer sub-channels (SC1 and SC3) is 25.71 mm. With that in mind, the Reynolds numbers reported for each of the subchannel flows reflects the hydraulic diameter of the respective subchannel.

Upon exiting the test section, the flow passes through the second diffuser connecting the rectangular test section to a 21.15 cm diameter tee, which is connected to both a vertical overflow section and an elbow shown in corner 1 in Figure 2. To prevent flow separation, the diffuser is designed with a length of 91.44 cm and a half angle of 3.51° , as literature suggests that shorter conical expansions with half angles of 5° and 4° caused flow separation [21]. The tee connects the diffuser with an overflow section that acts as a means to both fill the facility with working fluid and to degas it. The tee also connects with a 90° elbow that recirculates the flow back to the pump in corner 2 of Figure 2. The pump is selected based on the system pressure drop, which is determined using classical fluid dynamics relations accounting for both

major and minor losses [22]. To ensure a leak-tight setup, NBR 60-A DURO Nitrile gaskets are used throughout the tunnel with appropriate squeeze percentages [23]. Further details on the design of the facility are found in a previous work by Gonzalez [24].

2.2 Data Acquisition Setup

Flow velocimetry measurements are conducted using a mono PIV setup that includes a laser sheet generated by a dual-head DM30-527 Argon laser operating at a wavelength of 527 nm and a maximum power of 60 mJ/pulse. The measurement setup also includes four 12-bit dynamic range Phantom Micro M120 cameras with a maximum resolution of 1920×1920 pixels. Each camera is equipped with a Nikon 52 mm f/1.8D lens, and a LaVision Inc. 527 nm lens filter to help shield background noise and focus on light from the laser sheet. Additionally, Scheimpflug mounts are used on each camera to help fine-tune the focus and field of view, ensuring it is normal to the laser sheet. The seeder particles used in this tunnel are Conduct-O-Fil® SH400S20 silver-coated hollow glass spheres that are on average 13 μm in size. Raw images are processed using LaVision DaVis 8.4 software, where the images are passed through a time-series filter to subtract out unwanted noise. Using the filtered images, the velocity vectors are then calculated using a six-pass cross-correlation where the two initial passes are equipped with a 64×64 -pixel interrogation region, 1:1 square grid and 75% overlap. The latter four passes utilize a 32×32 -pixel interrogation region, with an adaptive grid and 75% overlap. The adaptive grid allows for greater accuracy in regions with strong velocity gradients. Generally, the data is also passed through a two-pass median filter to remove spurious vectors by removing them if their difference from the average is more than 1.5 standard deviation than that of its neighbors and replaces it if the difference from the average is less than 2.5 standard deviations from its neighbors. This filter removes further noise from the profiles.

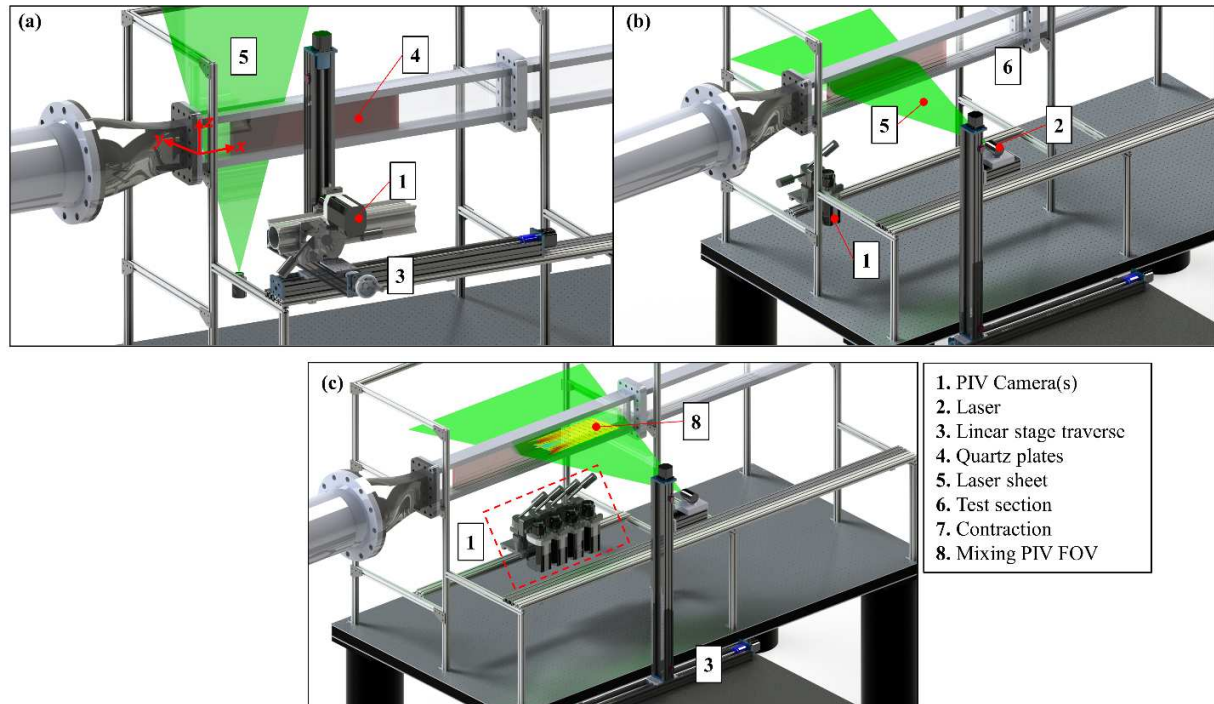


Figure 4. The mono-PIV experimental setup for (a) the inlet characterization in the transverse (xz) plane, (b) the inlet characterization in the spanwise (xy) plane, and (c) the mixing tests in the spanwise plane.

The inlet bulk velocity is characterized using a single camera and laser setup in the transverse (xz) plane and another in the spanwise (xy) plane. Figure 4 (a) illustrates the xz -plane setup, while the xy -plane setup is shown in Figure 4 (b). The xz -plane measurements are performed with a sampling frequency of 1 kHz for 2.778 s with scaling factor of 7.73241 pixels/mm, yielding a field of view of 91.05×135.53 mm, which starts ~ 61 mm from the physical inlet of the test section. The xy -plane measurements are performed with a sampling frequency of 600 Hz for 2.452 s with a scaling factor of 10.2119 pixels/mm, yielding a field of view of 188.02×85.39 mm, which starts ~ 62 mm from the physical inlet of the test section.

Figure 4 (c) illustrates the setup for the multi-regime hydraulic mixing studies. In this setup, four identical cameras view a laser sheet on the xy -plane along the transverse centerline ($z = 0$). Each camera is recording with a sampling frequency of 600 Hz for 2.563 s with a scaling factor of 11.5235 pixels/mm. The field of view each camera records is 166×60 mm with some amount of streamwise overlap between

each of the cameras (~0.6 hydraulic diameters). The first two cameras view the flow upstream of, and at the mixing region, and they encompass the entire spanwise view of the test section with a ~60 mm (~0.83 hydraulic diameters) wide field of view. The last two cameras view the flow development downstream of the mixing region, and due to physical/optical restraints, only accommodate ~40 mm (~0.55 hydraulic diameters) of the test section in the spanwise direction. This experimental limitation does not hinder the results, as only near-wall data downstream of the mixing phenomenon are missing, where the velocity profiles approach a fully mixed condition similar to the inlet profiles. The results discussed later in this paper help to validate this statement. The fields of view from each camera are stitched together in DaVis 8.4, where the stitching algorithm removes any peak ratios that are less than two, ensuring the best possible stitching. The total field of view consists of an area spanning 6.68 hydraulic diameters in the streamwise direction, beginning at a location 7.64 hydraulic diameters from the physical inlet of the test section. This configuration allows for the most reasonable tradeoff between temporal and spatial resolutions for the desired mixing profiles, and enabled data acquisition without significant requirements on memory usage.

Additionally, flow temperature measurements are performed using a type T thermocouple in conjunction with a National Instruments PXIe-4353 data acquisition unit. The thermocouple is calibrated using a crushed ice bath zero-point temperature reference. Calibrations are performed in-house and consist of 13 measurements and 12 trials in the range of 23.9 to 148.9 °C, enabling high-quality repeatable temperature measurements. The calibration setup incorporates an IsoTech calibration system consisting of a Calisto 2250 dry block temperature calibrator and MilliK precision data acquisition unit with a 935-14-61 platinum resistance thermometer as a reference probe. The calibrated thermocouple yielded a bias with a standard deviation of ± 0.509 °C and a precision uncertainty with a standard deviation of ± 0.146 °C. The total thermocouple uncertainty has a standard deviation of ± 0.53 °C with the highest uncertainty at 148.9 °C, which is a temperature that is both undesirable and unachievable in the MIR tunnel.

3. Inlet Flow Characterization

3.1 Bulk Flow Thermal Characteristics

Thermal energy is added to the working fluid via the pump; therefore, the steady operating temperature of the flow is dependent on the pump operating frequency (F). From experimental testing, the steady operating temperature in Eq. (1) is found to describe this relationship where the pump frequency is in units of Hz. It should also be noted that the thermal response time of the facility is quite long, especially compared to the hydrodynamic response time which is on the order of a few seconds. For reference, the expression quantifying the initial rate of temperature rise from these transient assessments is provided in Eq. (2), and reveals that even for the highest pump frequency operation ($F = 40$ Hz), the rate of temperature increase, or temperature response time, is 0.21 °C/min. The impact of temperature on the index of refraction is discussed in the next section, but is shown to be minimal, especially considering the thermal response time of the facility. Measuring the temperature during a test also accommodates temperature dependent fluid properties to be used in calculating the Reynolds number. Equations (3) and (4) are used for density and kinematic viscosity, respectively, and are taken from [25].

$$T(^{\circ}\text{C}) = 1.1029F + 15.8824 \quad (1)$$

$$\Delta T/\Delta t (^{\circ}\text{C}/\text{min}) = F^3 \times (3.31 \times 10^{-6}), \text{ for } 6 \text{ Hz} < F < 40 \text{ Hz} \quad (2)$$

$$\rho \left(\frac{\text{kg}}{\text{m}^3} \right) = (-0.00062314 T(^{\circ}\text{C}) + 0.84616) \times 10^3 \quad (3)$$

$$\nu \left(\frac{\text{m}^2}{\text{s}} \right) = (-10.9184 \ln(T(^{\circ}\text{C})) + 48.48063) \times 10^{-6} \quad (4)$$

Being an MIR tunnel, it should be noted that some characterization efforts are directed towards quantifying the index of refraction (IOR) mismatch due to temperature rise. Sabharwall et al. [26] did a Monte Carlo-based (global) sensitivity analysis on that same topic for the MIR facility at Idaho National Laboratory, which also uses Drakeol[®] 5 oil and quartz as a means of achieving a matched index of refraction. The analysis considered all possible distances between the oil, quartz, test section walls, and camera focus as well as the mineral oil temperature. The Monte Carlo-based sensitivity analysis followed

steps outlined by Saltelli [27]. The parameters were fed into SimLab 2.2 software [28] with an uncertainty and a range of values for each parameter. The software then randomly generated datasets based on the input parameters, successfully implementing the Monte Carlo functionality into the analysis. The generated datasets were then fed to a MATLAB program that calculates the mean error in velocity due to IOR mismatch from temperature changes. The MATLAB outputs are then fed back into SimLab 2.2 to estimate the velocity measurement errors due to random temperature changes. The velocity measurement error in that study is defined using the variance-based methods used in their MATLAB script and outlined in Sobol's work [29, 30], where the study accounted for the scaling factor, pixel displacement, and time between image pairs used for the PIV measurement. Sabharwall's study showed that for a temperature uncertainty of ± 1 °C, the velocity measurement error was less than 0.0025%. It also showed a linear relation between velocity measurement error and temperature uncertainty, where an uncertainty of ± 0.01 °C yielded an average velocity measurement error on the order of 10^{-5} %; therefore it would take a temperature error of ± 40 °C (hence a temperature difference between quartz and mineral oil of 40 °C) to reach a velocity measurement error of 0.1% per calculations by Weiss et al. [3131]

The low measurement error can be explained by the lack of mismatch between a change in the IORs of Drakeol® 5 and quartz in general. The quartz IOR at a 527 nm wavelength, which is the wavelength of the laser used for PIV measurements in this work, could be estimated between 20 and 30 °C using the linear relation shown in Eq. (5) per data provided in classical literature [32]. The Drakeol® 5 IOR were measured by Budwig and Westin between 20 and 35 °C and can be estimated using the linear relation shown in Eq. (6) [25]. Comparing IORs from both relations at different temperatures within the range of 20 and 30 °C provide a maximum IOR mismatch less than 0.4% between the oil and quartz. With this information, it is understood that although temperature control is highly desirable, the IOR mismatch between Drakeol® 5 allows for serious leeway in the precision of said control, or complete lack-thereof. A temperature rise from 30 °C to 60 °C, which would take at least 2.38 hours of continuous operation, yields negligible changes in the quartz index of refraction, and less than 1% change in the oil's index of

refraction. This motivates the authors to state that the intrinsic temperature rise in the system is not a major concern for maintaining the MIR phenomenon.

$$n_{Quartz} = 0.0000010159 T(^{\circ}\text{C}) + 1.4609 \quad (5)$$

$$n_{Oil} = -0.00035909 T(^{\circ}\text{C}) + 1.4674 \quad (6)$$

3.2 Inlet Velocity

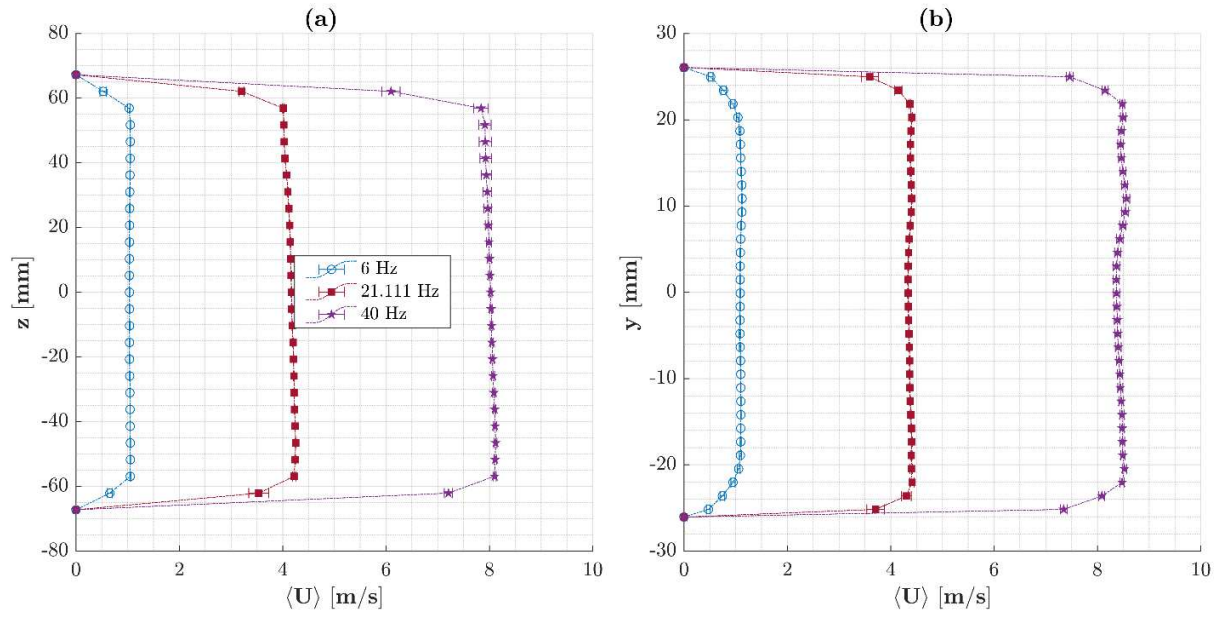


Figure 5. Ensemble-averaged inlet profiles of the minimum and maximum velocities in the (a) transverse and (b) spanwise planes. Blue traces correspond to the lowest tunnel operation limit and the purple traces correspond to the highest operation limit of the tunnel, while the red traces correspond to an intermediate operation condition for the tunnel.

The inlet bulk velocity of the oil in the test section of the tunnel can be represented as a function of the pump frequency in Hz per Eq. (7). A detailed explanation of the derivation of this equation can be found in Weiss et al. [31] alongside inlet velocity profiles ~ 1.25 hydraulic diameters from the physical inlet of the test section (~ 1.1 hydraulic diameters upstream of the leading edge of the quartz plates). For this study, another set of inlet velocity profiles are provided ~ 1.652 hydraulic diameters from the physical inlet of the test section, and are illustrated in Figure 5 (a) and (b) for the transverse and spanwise planes respectively. The error bars shown for the tunnel operation limits (blue and purple traces) represent a total

uncertainty that accounts for system error (bias) and random (precision) error. The error bars shown for the intermediate pump frequency of 21.111 Hz (red traces) are only representative of bias because it represents data collected from one trial only. Generally, the uncertainties tend to increase in magnitude with increasing U_b , but they remain minimal across the operation limits of the tunnel (within 5%).

$$U_b = 0.2122F - 0.1906 (\pm 3.92\%), \quad 6 \text{ Hz} \leq F \leq 40 \text{ Hz} \quad (7)$$

This inlet velocity characterization shows that, within a 3.92% uncertainty, the MIR tunnel is capable of replicating flows between 1.08 m/s and 8.19 m/s. Coupled with the bulk flow thermal characterization discussed earlier, the main channel is capable of Reynolds numbers between 5603 and 44,173 assuming the flow temperature remains within 23 °C to 24 °C, which is within the bounds of the flow temperature for the experiments that are conducted. In that same temperature range, the outer sub-channels can replicate Reynolds numbers between 2644 and 20,844, while the inner sub-channel is capable of Reynolds numbers between 1824 and 14,382. The lower Reynolds number capabilities of 1824 and 2644 for the inner and outer sub-channels respectively are promising for efforts towards studying single-phase flows in transitional regimes. Such studies are valuable for providing a more holistic understanding of the transition between laminarity and turbulence, potentially allowing for the development of better closure models [33].

3.3 Inlet Turbulence Intensity and Flow Angularity

Plesniak et al [34] demonstrates that even minor changes to the inlet conditions can yield significant changes in 2nd order statistics such as Reynolds stresses in the near-field of a mixing layer. As such, it is important to have a deep understanding of inlet conditions, particularly more complex conditions such as the turbulence intensity and angularity of the flow. Figure 6 (a) and (b) correspond to the turbulence intensity profiles in the transverse and spanwise planes, respectively at multiple bulk pump operation limits, and by extension multiple U_b . The turbulence intensities show uniform distributions that are

characteristic of flow in channels, where flat profiles are observed in the free stream with maxima near the walls of the channels. On average, the turbulence intensity in both planes is 2.53 – 5.24%.

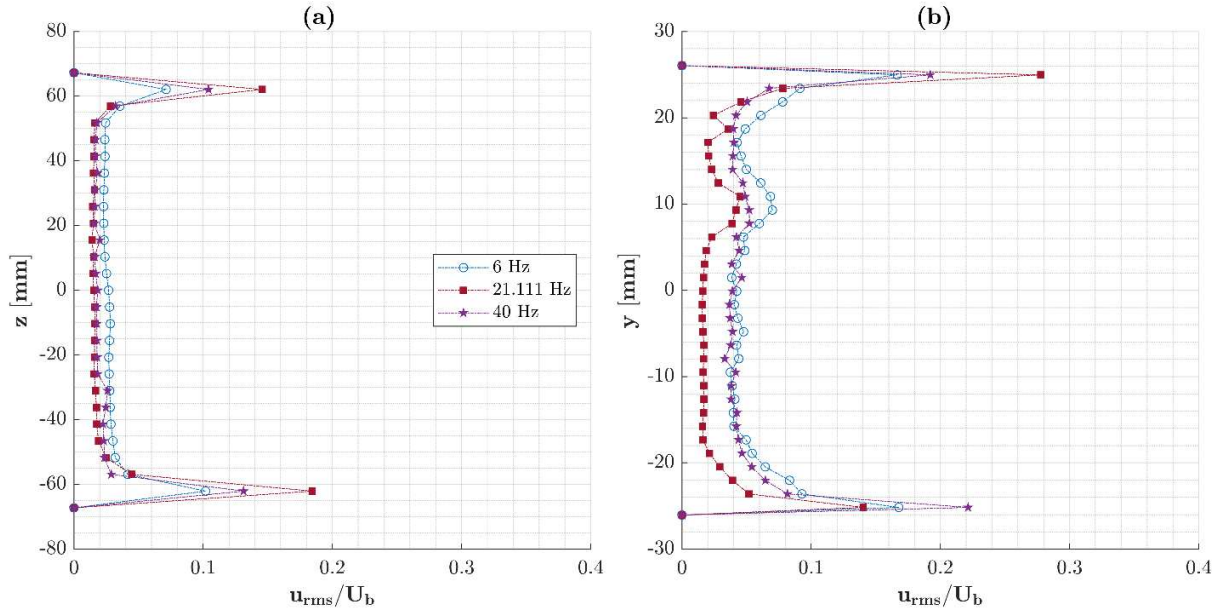


Figure 6. Time-averaged inlet turbulence intensities in the (a) transverse and (b) spanwise planes.

The higher turbulence intensities in the spanwise plane are attributed to higher noise imposed by the relatively smaller viewing area, thicker acrylic walls relative to the side walls, and potentially some dust particulates settling on the bottom of the test section. All the aforementioned noise causations contribute to increased noise that can throw-off the pixel intensity-based PIV processing algorithms. A median filter is implemented in the spanwise plane to help denoise the data. The filter scans for vectors whose difference to the average is greater than $2\times$ the root mean square of its neighbors and softens them by subtracting 75% of the standard deviation between them and their neighbors. The filter is based on PIV filtration practices recommended by Wieneke [35]. It should be noted that there is a noticeable asymmetry between the peak turbulence intensities at the top and bottom walls of the test section. This is attributed to a small gasket piece that adheres to the upper portion of the inner quartz wall, causing higher turbulence intensities in the upper walls of the test section as demonstrated by Figure 6 (b). These details might seem

like typical experimental hardships, but they are valuable for future validation work that might consider data generated in this tunnel and may provide potential explanations for any discrepancies.

Angular studies of the flow quantify the angle formed by the streamwise and transverse velocity components (θ_{UW}) and the streamwise and spanwise velocity components (θ_{UV}) at the inlet. These angles provide a measure of how unidirectional the flow is at the inlet and can be used as metrics to back-calculate the transverse and spanwise velocity components at the inlet given the streamwise inlet velocity distributions in Figure 5 (a) and (b) respectively. In the bulk flow, the maximum θ_{UW} is found to be below 1.27° , while θ_{UV} has a maximum of 1.29° . This allows the authors to confidently state that the inlet velocity profile is streamwise-unidirectional to within $\pm 1.5^\circ$.

Finally, all the inlet velocimetry data are checked for statistical convergence by calculating a convergence error criterion (ϵ) shown in Eq. (8). First and second-order statistics are checked in both the xz plane and xy plane, and the results are summarized in Table 1. All parameters are statistically convergent to within very low error criteria. The first order statistics are convergent to within a 10^{-5} criterion, which is comparable to what one would expect from high quality CFD residuals. The lowest convergence is found with the shear Reynolds stresses $\langle uv \rangle$ and $\langle uw \rangle$, but even those are convergent to within 10^{-3} , and are hence of a high enough sampling to serve as validation metrics. The convergence criteria are beneficial to CFD validation studies as they provide modelers with a quantifiable measure of trust in the experimental data.

$$\epsilon_n = \frac{|X_n - X_{n-1}|}{X_n}, \quad \begin{cases} X = \text{any parameter of choice} \\ n = 2 \dots N \text{ (maximum number of PIV frames)} \end{cases} \quad (8)$$

Table 1. The statistical convergence error criteria for multiple inlet velocimetry parameters.

| Parameter | Significance | Spanwise Plane | Transverse Plane |
|----------------------|---|-----------------------|-----------------------|
| $\langle U \rangle$ | Figure 4 | 2×10^{-5} | 7.5×10^{-5} |
| u_{rms} | Figure 5 | 3.89×10^{-4} | 9.44×10^{-5} |
| $\langle uu \rangle$ | 2 nd order statistics fidelity | 7.79×10^{-4} | 1.89×10^{-4} |
| $\langle uv \rangle$ | 2 nd order statistics fidelity | 2.77×10^{-3} | - |
| $\langle uw \rangle$ | 2 nd order statistics fidelity | - | 4.65×10^{-3} |
| $\langle vv \rangle$ | 2 nd order statistics fidelity | 8.3×10^{-5} | - |
| $\langle ww \rangle$ | 2 nd order statistics fidelity | - | 2.28×10^{-4} |

With the insights gained from the inlet characterization of the tunnel, a multi-regime hydraulic mixing study is performed using the existing test section with the three rectangular sub-channels. The results section discusses seven cases with the respective U_b of 1.08, 1.88, 2.69, 3.49, 5.09, 6.69, and 8.3 m/s with room temperatures in the range of 23 °C to 24 °C, resulting in multiple cases with differing flow regimes and Reynolds numbers in each of the sub-channels.

4. Results & Discussion

The experimental setup shown in Figure 4 (c) is utilized with the data acquisition equipment detailed in section 2.2 to investigate mixing from three rectangular channels. The investigations included the test cases outlined in Table 2. The different Re combinations between the inner and outer sub-channels allow for an understanding of mixing with respect to variations in Re and flow regimes. Note that the Re ratio between the outer and inner sub-channels is practically constant (0.69) across all cases, therefore any variations in the flow behavior cannot be attributed back to a velocity or temperature ratio, but to a change in the flow regime. Although cases 3-7 are all turbulent mixing cases, the Re of the main channels (and therein the sub-channels) differ by up to 3×10^4 , and are treated as varying from “slightly turbulent” (cases 3 and 4) to “highly turbulent” (case 7). As such, the following subsections of this paper

are divided to capture the variation between slightly and highly turbulent flows, and then separately observe the effects of flow regime variations. It should be noted that the same physical phenomena are encountered across all cases. As such, the physical phenomena are heavily discussed for the cases discussing the Reynolds number variation effects, leaving a more straightforward discussion for the cases investigating flow regime variation effects.

Table 2. The different test cases for the mixing studies. Cases 1 and 2 correspond to multi-regime mixing, while the rest of the cases correspond to turbulent mixing with increasing Reynolds numbers. SC1 and SC3 correspond to the outer sub-channels, while SC2 corresponds to the inner sub-channel per Figure 3.

| Test Case / U_b | Re | | | Fluid Temperature | Regime Combination |
|----------------------|--------------|-----------|---------|-------------------|------------------------|
| | Main Channel | SC1 & SC3 | SC2 | | |
| 1 / 1.08 m/s | ~5,603 | ~2,644 | ~1,824 | 23.4 – 23.5 °C | Transitional-Laminar |
| 2 / 1.88 m/s | ~9,755 | ~4,603 | ~3,176 | 23.4 – 23.5 °C | Turbulent-Transitional |
| 3 / 2.69 m/s | ~13,946 | ~6,581 | ~4,540 | 23.5 – 23.6 °C | Turbulent-Turbulent |
| 4 / 3.49 m/s | ~18,292 | ~8,632 | ~5,956 | 23.8 – 23.9 °C | Turbulent-Turbulent |
| 5 / 5.09 m/s | ~26,746 | ~12,620 | ~8,708 | 23.8 – 24.1 °C * | Turbulent-Turbulent |
| 6 / 6.69 m/s | ~35,349 | ~16,680 | ~11,509 | ~23.8 – 24.4 °C * | Turbulent-Turbulent |
| 7 / 8.3 m/s | ~44,173 | ~20,844 | ~14,382 | ~23.8 – 24.9 °C * | Turbulent-Turbulent |

* Estimated temperature range based on a 5-minute experiment (Equation 2) with an initial temperature of 23.8 °C.

4.1 Reynolds Number Variation Effects – 1st Order Statistics

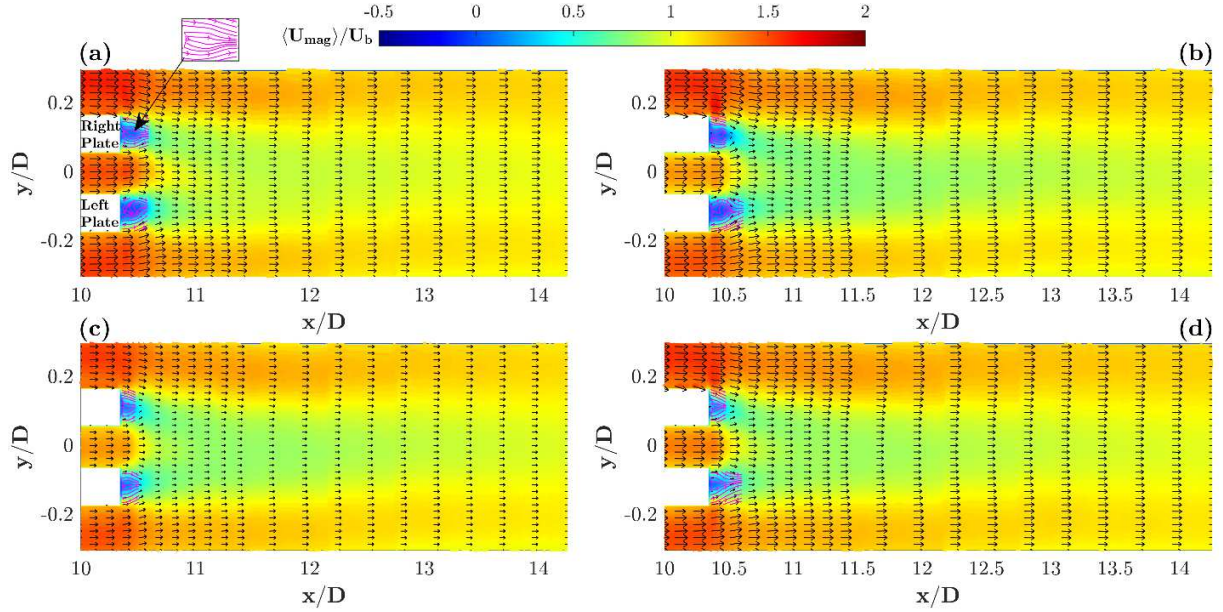


Figure 7. Contour plots of $\langle U_{mag} \rangle$ normalized by U_b for (a) case 4, (b) case 5, (c) case 6 and (d) case 7, showing the Reynolds number variation effects on the spatial distribution of the velocity. The right and left (perceptively top and bottom) quartz plates are masked with white boxes respectively spanning $0.17 \leq y/D \leq 0.06$ and $-0.06 \leq y/D \leq -0.17$ in the spanwise direction, and both spanning $10 \leq x/D \leq 10.35$ in the streamwise direction. Recirculation pockets are highlighted with magenta streamlines directly downstream of the walls.

First order statistics observations consider analyses of the time-average streamwise component of the velocity $\langle U \rangle$ (normalized by U_b). The spanwise velocity component $\langle V \rangle$ is neglected in this analysis as miniscule variations are observed with respect to Re variation. Figure 7 (a-d) show the respective contour plots for cases 4-7 **respectively**, illustrating the spatial evolution of the normalized velocity magnitude $\langle U_{mag} \rangle / U_b$. The contour plots look very similar, with the most notable distinction being the recirculation pockets softening as the Re progresses from the slightly turbulent flow in Figure 7 (a) to the highly turbulent flow in Figure 7 (d). The recirculation pockets are illustrated on the figures with magenta streamlines.

In each respective case, the flows in each sub-channel begin with similar $\langle U_{mag} \rangle / U_b$ until the sub-channel walls (quartz plates) end abruptly at $x/D = 10.35$, at which the flows from the outer sub-

channels exhibit a fairly symmetric behavior that mimics the flow features that can be found in the presence of a backward facing step. Much like backward facing step flow, a recirculation pocket can be found directly downstream of the walls' ends, and a separated shear layer is found moving inwards (towards the inner sub-channel) as the flow progresses further downstream. The recirculation pockets are small in this flow scenario, meaning that the flows from the outer sub-channels, or outer flows, reattach to the inner flow with very small recirculation lengths. The recirculation lengths are in the range of 0.02 – 0.15 hydraulic diameters, and although they do not vary linearly with Re , the lengths generally decreased with increasing Re . Although literature is inconsistent when it comes to quantifying exact reattachment lengths of backward facing step flows [36, 37], the general decrease in this work's recirculation lengths with increasing Re is contradictory to the general notion that the opposite is expected to occur [38]. This contradiction is of course expected due to the fact that the recirculation length is also affected by the inner channel flow, which is lacking in all backward facing step flows.

The inner flow essentially acts as a moving base in the backward facing step, prompting counter-rotating pairs directly downstream of the walls as evidenced by the opposing vectors on each side of either wall. Additionally, the availability of opposing velocity vectors on each side of the wall forces the recirculation pocket lengths to be shorter than they would in a backwards facing step. As the inner flow increases with increasing Re , so will the magnitude of its velocity vectors, leading to smaller recirculation pockets due to the increased resistance to the outer flows. This eventually yields smaller recirculation lengths with increasing Re in this flow scenario. This is consistent with observations from flows around bluff objects, wherein the recirculation bubble tends to decrease in size with increasing Re [39].

The fact that the inner flow is sandwiched between the two outer flows means that the inner flow possesses two shear layers as opposed to the one layer ~~each~~ that ~~each of~~ the outer flows exhibit. Those shear layers can be observed in Figure 7 (a) – (d), where they are represented by the yellow outlines ($\langle U_{mag} \rangle / U_b \sim 1$) surrounding each of the flows exiting the sub-channels. This shearing surrounding the inner flow leads to a notable reduction in its velocity upon exiting the inner sub-channel as the

momentum of the inner flow is being stripped by two shear layers, leaving the outer flows with higher velocities. This notion is backed by observing the shear layer lengths, where the lengths of the inner shear layers do not extend beyond 11 hydraulic diameters, while the shear layers of the outer flows can be observed to extend past the field of view. As all flows eventually progress downstream, the velocity vectors across the spanwise depth of the channel tend to equalize as the flow approaches a fully developed behavior. It should be noted that additional downstream length is necessary to truly observe fully developed flow, and hydrodynamic entrance length cannot be quantified with the current data.

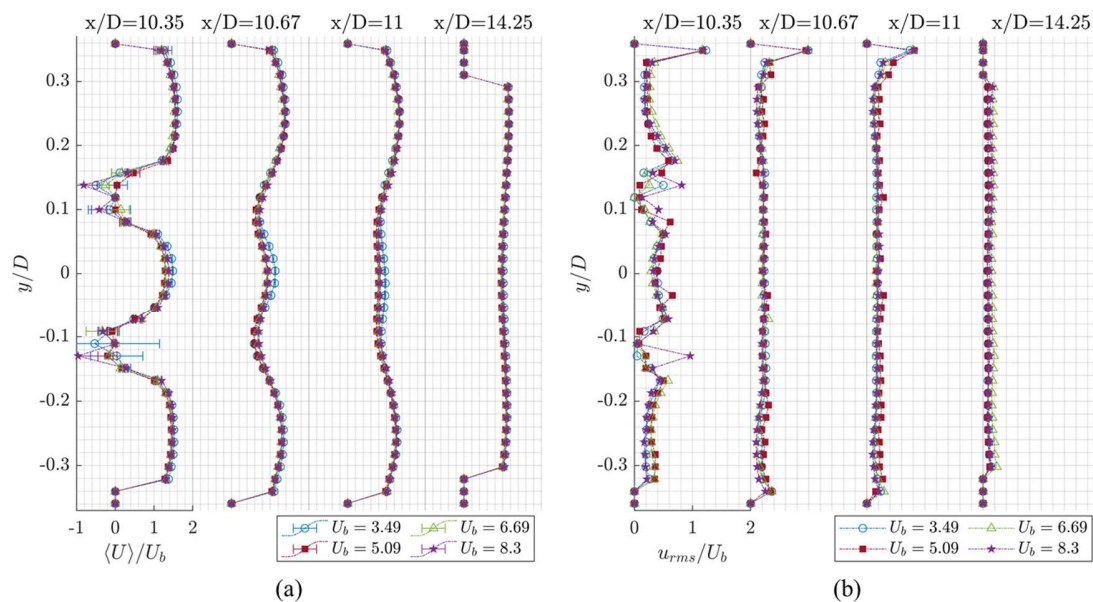


Figure 8. Spanwise profiles of (a) $\langle U \rangle / U_b$ and (b) turbulence intensities at multiple streamwise hydraulic diameters and multiple cases (cases 4-7) showing the evolution of velocity and turbulence intensity due to Reynolds number variation.

The spanwise profiles provided in Figure 8 (a) show the evolution of $\langle U \rangle / U_b$ as the flow progresses from the start of the converging region at the sub-channel outlets ($x/D = 10.35$) to somewhere around the center of the mixing/merging region ($x/D = 10.67$), and then to the combined region where the flows recombine and further develop. Figure 8 (b) shows the evolution of turbulence intensities throughout the mixing phenomenon and are of value to future turbulence model validation studies. In general, the turbulence intensity remains low and comparable across all cases and tends to be at a maximum at the

start of the converging region. This evolution of the flow fields strongly resembles the mixing of parallel jet flows [7, 40], and is extremely similar to existing results of turbulent mixing in confined rectangular channels [41]. At the sub-channel outlets, the results in Figure 8 (a) indicate that the velocity across all cases for each sub-channel are very similar, and the velocity ratio between the inner flow and the outer flows (U_{in}/U_{out}) is quantified as $\sim 0.9 (\pm 0.08)$. As such, it is appropriate to present all cases as quasi-isovelocity mixing with varying Re magnitudes between the inner flow and the outer flows.

In all cases, an identical behavior is present where the velocity in the converging region decays as it approaches the mixing region, with the most drastic decay being present in the inner flow due to having twice the shear layers that either of the outer flows exhibit. The flows then continue towards the combined region where they approach a fully developed channel flow behavior. This is similar to triple-jet mixing [7] except for the availability of prominent negative streamwise velocities where the sub-channel walls would be prior to the converging region, indicating the presence of the recirculation pockets. Prominent recirculation pockets are only characteristic of plane jets [40, 42], as three-dimensional flows tend to have very little negative velocity between the jets due to the absence of channel walls bounding the flows [43, 44]. The availability of walls in this confined flow scenario makes it more like plane jets, where the shear layers of the inner flow cause ~~negative pressure between the flows~~ adverse pressure gradients, yielding recirculation pockets that enhance the convergence of the flows towards a symmetry line ($y/D = 0$). In other words, bounding the flows with channel walls enhances the mixing characteristics as it enables a faster approach to the combined region.

4.2 Reynolds Number Variation Effects – 2nd Order Statistics

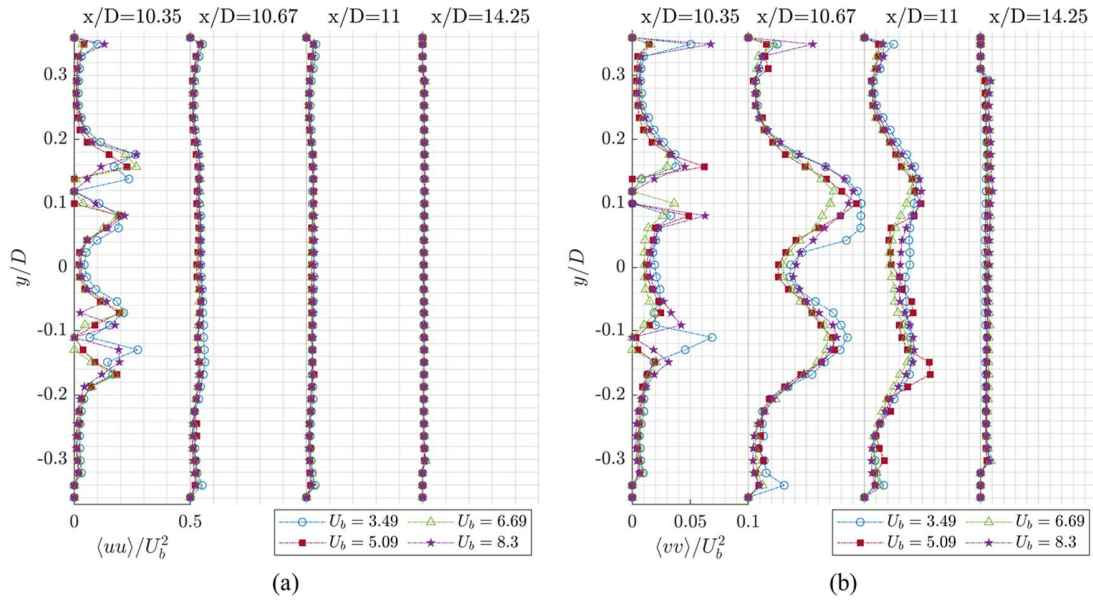


Figure 9. Spanwise profiles of (a) $\langle uu \rangle / U_b^2$ and (b) $\langle vv \rangle / U_b^2$ at multiple streamwise hydraulic diameters and multiple cases showing the evolution of the normal Reynolds stresses due to Reynolds number variation.

A deeper understanding of the flow behavior can be derived by analyzing the Reynolds stress profiles, which can help isolate and identify the energy contributions in the flow field. Figure 9 (a) and (b) shows spanwise profiles of the normal Reynolds stresses in the streamwise $\langle uu \rangle / U_b^2$ and spanwise $\langle vv \rangle / U_b^2$ directions, respectively (note both are normalized by U_b^2). The $\langle uu \rangle / U_b^2$ profiles in Figure 9 (a) are most prominent in the converging region at $x/D = 10.35$, where peaks are seen in locations where shear layers are expected for the outer flows and the inner flow. Consistent with previous observations, the inner flow exhibits two peaks at locations that correspond to its shear layers, while each of the outer flows only exhibit one prominent peak that correspond to the shear layer on the inside (near the center) of the field of view. A less prominent $\langle uu \rangle$ peak is observable near the walls, which is expected as the wall friction causes drag that promotes elevated stresses near the wall. It should be noted that the peak near the left wall (at $y/D \approx -0.15$ in the $x/D = 10.35$ profile) is smoothed out due to the aforementioned experimental artifacts, but its existence is highly trivial and should be expected nonetheless based on

existing literature and current understanding of confined mixing flows [41]. The $\langle vv \rangle / U_b^2$ profiles in Figure 9 (b) exhibit a similar behavior to the $\langle uu \rangle / U_b^2$ profiles at $x/D = 10.35$, albeit with significantly lower magnitudes. The smaller $\langle vv \rangle / U_b^2$ magnitudes are indicative of the strong unidirectionality of the flows upon exiting their sub-channels, which become less unidirectional as the flow progresses downstream.

The $\langle uu \rangle / U_b^2$ magnitudes tend to decrease as the flows progress downstream of the merging region to values that are comparable to, or smaller than, the $\langle vv \rangle / U_b^2$ magnitudes. It is interesting to note that spanwise stresses become more dominant in the mixing region at $x/D = 10.67$. This can be attributed to the inner and outer flows attempting to merge as the flow passes the recirculation pockets, where the velocity vectors of the outer flows move towards the inner flow and cause an increase in spanwise velocities that prompt increased $\langle vv \rangle / U_b^2$ magnitudes. The prominent $\langle vv \rangle / U_b^2$ peaks near the center of the $x/D = 10.67$ profiles signify the locations of the mixing layers, where two are needed for the two outer flows to merge with the inner flow. The asymmetries, most noticeable in case 4, are determined to be characteristic of experimental artifacts, and not characteristic of the actual flow physics. Although exact locations of the mixing layers are not viable with this data set, it can be deduced that the mixing layers lie around 0.1 hydraulic diameters from the spanwise centerline. This means that mixing layers are downstream of the walls and are not directly parallel with the leading edges of the plates, which distinguishes them from the shear layers that can be observed in the shear Reynolds stress $\langle uv \rangle / U_b^2$ profiles at $x/D = 10.67$.

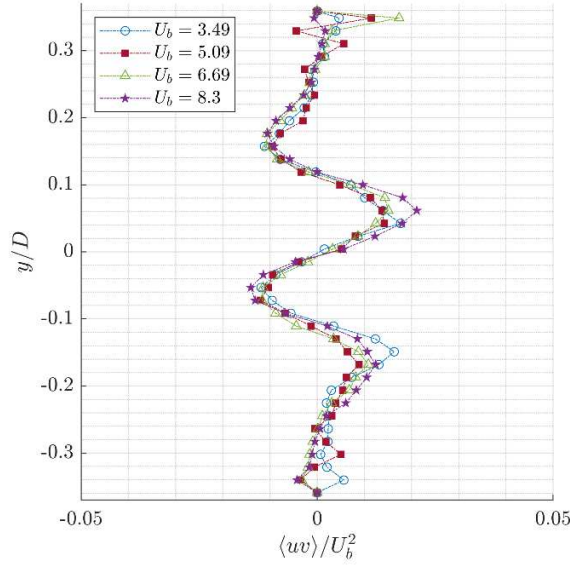


Figure 10. Spanwise profiles of $\langle uv \rangle / U_b^2$ at multiple streamwise hydraulic diameters and multiple cases showing the evolution of the shear Reynolds stresses due to Reynolds number variation.

Figure 10 shows the $\langle uv \rangle / U_b^2$ profiles at $x/D = 10.67$ for the respective cases 4-7. Once again, the shapes and magnitudes of those profiles are nearly identical for all the cases. Contrary to the peaks in the $\langle vv \rangle / U_b^2$ profiles, the peaks in this profile are indicative of the shear layer locations instead of mixing layers. As previously discussed, the inner flow exhibits two shear layers, while the outer flows each get one shear layer, which translates to four distinct peaks in this $\langle uv \rangle / U_b^2$ profile. Those peaks can be seen at $y/D = 0.15, -0.15$ for the outer shear layers, and $y/D = 0.05, -0.05$ for the inner shear layers. It is interesting to note that the mixing layers observed in Figure 9 (b) lie halfway between each inner-outer shear layer pair at $y/D = 0.1, -0.1$. Mixing layers are known to form at the exit of the flows [45], which is due to the presence of a velocity gradient at that streamwise location. Similarly, the availability of the mixing layer halfway between each shear layer pair is likely because the most significant velocity gradient would be present at that spanwise location. While intriguing, these results may be characteristic to this specific MIR tunnel, as the Reynolds stress distributions in the mixing region are sensitive to initial conditions [34]. Nonetheless, the distance between each inner-outer layer pair in the $\langle uv \rangle / U_b^2$ profiles should denote the mixing layer thickness, which seems to be relatively constant, spanning 0.1 hydraulic

diameters across all Re variations shown in Figure 9 (b). Although the thicknesses of the mixing layers can be estimated by observing the $\langle uv \rangle / U_b^2$ and $\langle vv \rangle / U_b^2$ profiles, the length of said mixing layers would likely require an analysis of the streamwise centerline velocity decay, which is discussed in the next section.

4.3 Reynolds Number Variation Effects – Velocity Decay

Much like jet flows, the inner and outer flows expand as they exit their confined sub-channels (nozzles), and a higher centerline velocity (U_{cl}) decay is indicative of enhanced mixing characteristics with the surrounding quiescent fluid [7]. Streamwise decay of U_{cl} for each sub-channel is illustrated in Figure 11, where U_{cl} is the time-averaged centerline velocity at each streamwise location, and U_{max} is the maximum outlet velocity of flows from each of the sub-channels, as measured at $y/D \approx 0.25, -0.25$ for SC1 and SC3, respectively, and at $y/D \approx 0$ for SC2. U_{cl} is tracked by finding the centerline velocity at each x/D location at the aforementioned y/D locations for each of the sub-channels.

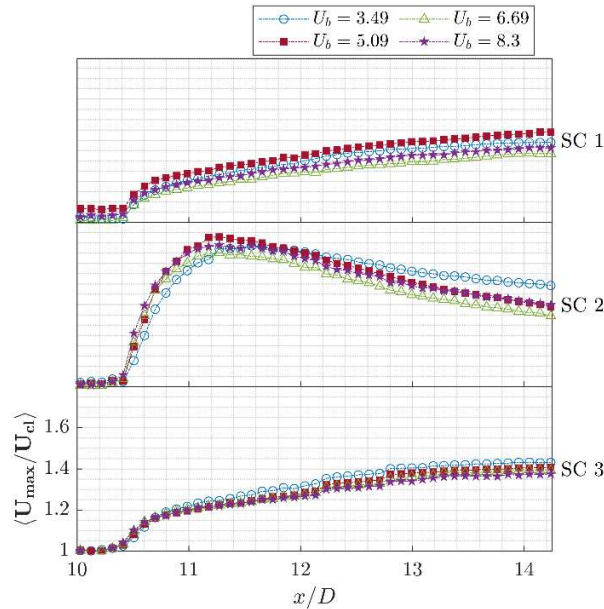


Figure 11. Streamwise decay $\langle U_{max}/U_{cl} \rangle$ of flows from cases 4-7 in each sub-channel, where SC1 corresponds to the right sub-channel (top sub-channel in Figure 7), SC2 corresponds to the center sub-channel, and SC3 corresponds to the left sub-channel (bottom sub-channel in Figure 7)

The time-averaged velocity decay $\langle U_{max}/U_{cl} \rangle$ profiles in Figure 11 show that the $\langle U_{max} \rangle \approx \langle U_{cl} \rangle$ up to the sub-channel outlets at $x/D = 10.35$, after which the velocity decay increases as a result of the flows expanding into the larger cross section. The decay rate, or the slope by which the velocity decays, is explained by considering the momentum transfer between the flows. As previously noted, the inner flow is surrounded by two shear layers and subsequently two mixing layers, as opposed to the outer flows, each of which neighbors only one shear and one mixing layer. As such, averaging across cases 4-7, the inner flow has the steepest slope of ~ 1.3 , as opposed to the relatively softer slope of ~ 0.38 for the outer flows. Literature shows decay rates ranging from as low as ~ 0.09 for round jet with slot lobes mixing with a cross flow [46], to ~ 0.18 for jets issuing out of triangular nozzles [4], and as high as ~ 0.21 for jets issuing out of rectangular nozzles [47]. This demonstrates superior mixing in this flow configuration, but only because of its confined nature. The fact that the outer flows are each bounded by a wall that continues after the flows exit their respective sub-channels, forces enhanced mixing as the flows can only expand towards the inner flow, which strongly assists the mixing phenomenon. In mixing scenarios with multiple jets, the flows expand towards and away from the inner flow, decreasing the mixing as there are no constraints limiting spreading of the outer flows and forcing them to mix with the inner flow.

The inner flow decay profile shown in Figure 11 exhibits a unique behavior wherein the decay rate varies as the flow progresses downstream. The outer flows possess a jet-like behavior where the velocity decays linearly at a relatively constant rate. The inner flow on the other hand experiences a steep decay upon exiting due to the strong influence from its two shear layers stripping momentum from it, which leads to the steep decay. The decay however reaches a peak, after which $\langle U_{cl} \rangle$ increases, causing a velocity growth wherein the inner flow catches up with the outer flows in the combined region. Across cases 4-7, the inner flow decay peaks at $x/D \approx 11.35$, which could denote the location where all the flows begin to combine as a single flow. The distance between the end of the recirculation pockets and the combined point signifies the length of the mixing layer, which would be in the range of $0.98 - 0.85$ hydraulic diameters for cases 4-7.

4.4 Flow Regime Variation Effects – 1st Order Statistics

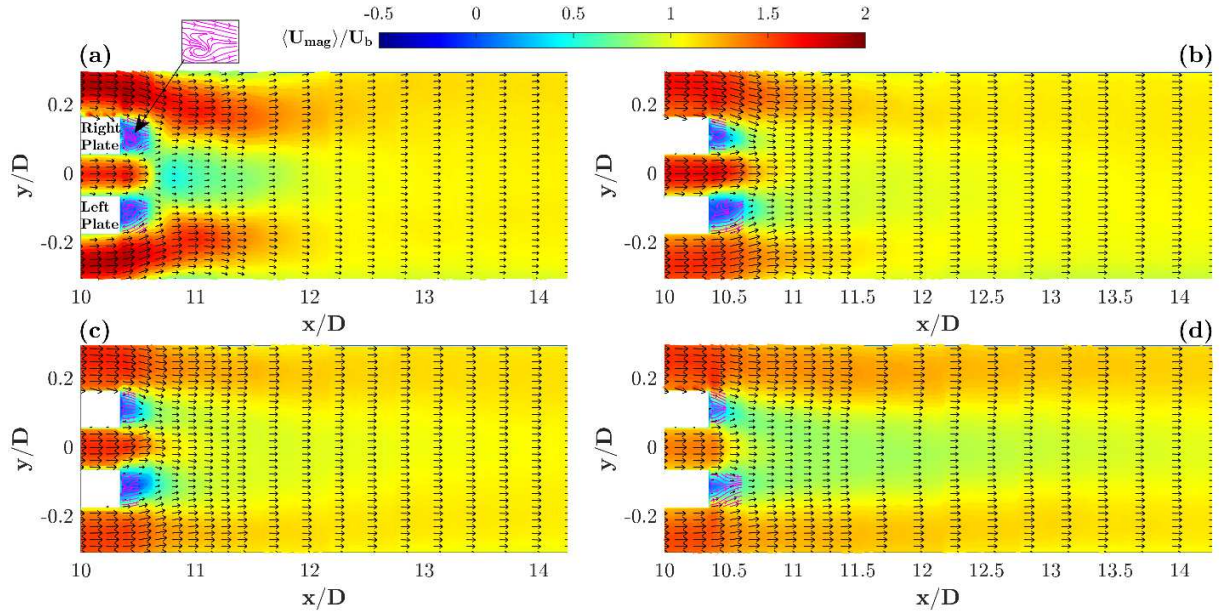


Figure 12. Contour plots of $\langle U_{mag} \rangle$ normalized by U_b for (a) case 1, (b) case 2, (c) case 3 and (d) case 7, showing the flow regime variation effects on the spatial distribution of the velocity. The inner-outer regime pair for case 1 is laminar-transition, transition-turbulent for case 2, slightly turbulent for case 3 and highly turbulent for case 7. Recirculation pockets are highlighted with magenta streamlines directly downstream of the plates.

Although the Re variation analyses showed that a change in Re in each sub-channel does not contribute to significant changes since the Re ratio remained the same, the cases analyzed have the same flow regime.

A similar set of analyses to the one discussed earlier is therefore carried out to demonstrate the effects of flow regime variation effects. This new set of analyses considers flow regime variations between the inner flow and the outer flows, and they consist of data from cases 1-3. The analyses also include the previously discussed results of case 7 to further enhance the discussions that follow. Figure 12 (a-d) show the respective contour plots of the velocity magnitude $\langle U_{mag} \rangle / U_b$ for cases 1-3 and 7, respectively. The recirculation lengths of case 1 and 2 are ~ 0.145 , while cases 3 and 7 are ~ 0.02 and ~ 0.05 , respectively. The trend of generally decreasing recirculation lengths due to increasing Re remains true in the analyses, but they are largest in the laminar-transition mixing (case 1) and the transition-turbulent mixing (case 2).

Case 1 shown in Figure 12 (a) is the most unique case, because although the Re ratio between the sub-channels is the same as all the other cases (~ 0.69), the flow field is different than all the other cases. The mixing region ($x/D = 10.67$) is particularly interesting as the inner flow experiences significant velocity decay compared to other cases. The outer flows also seem to converge significantly quicker than any other case, which is likely due to the aggressive velocity decay experienced by the inner flow. This qualitatively demonstrates the enhanced mixing characteristics of multi-regime mixing. The laminar inner flow decays to nearly a third of its velocity upon exiting the converging region at the end of the recirculation pockets, after which the outer flows can easily overcome the momentum of the inner flow and reach an earlier combined point than any of the other cases.

Case 2 shown in Figure 12 (b) shows transition-turbulent mixing, but although it is still technically multi-regime mixing, its effects are less prominent than case 1, and it strongly resembles the behavior observed in the turbulent mixing of case 3 in Figure 12 (c) and all other turbulent mixing cases presented earlier. Qualitatively, transition-turbulent mixing is synonymous with turbulent mixing, which could be because chaotic multi-scale behavior is observed in transition and turbulent flows alike, or it could be due to the lack of understanding when it comes to transitioning flows [33]. It is likely more applicable to describe the inner flow in case 1 as transition once it reaches the mixing region, instead of classifying the inner flow of case 2 as transition superficially based on its Re .

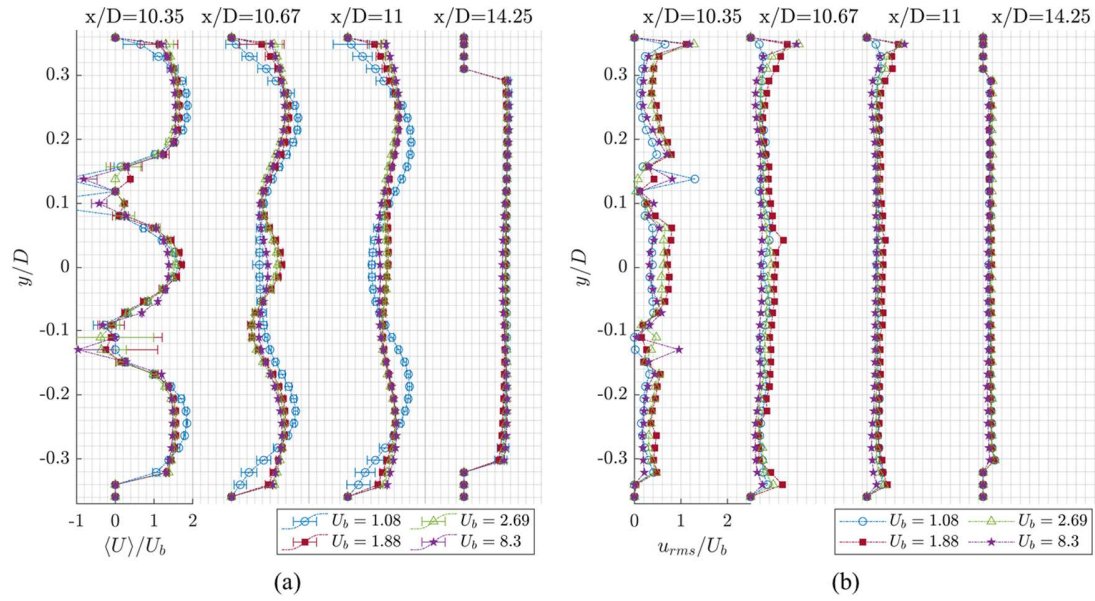


Figure 13. Spanwise profiles of (a) $\langle U \rangle / U_b$ and (b) turbulence intensities at multiple streamwise hydraulic diameters and multiple cases (cases 1-3 and 7) showing the evolution of velocity and turbulence intensity due to flow regime variation.

The spanwise velocity profiles in Figure 13 (a) show the streamwise evolution of the $\langle U \rangle / U_b$ across cases 1-3 ($U_b = 1.08-2.69$) and case 7 ($U_b = 8.3$). Velocities are comparable across all cases upon exiting at the beginning of the converging region ($x/D = 10.35$), but distinctions arise in case 1 as the flow progresses to the mixing region ($x/D = 10.67$) and eventually into the combined region. Firstly, the significant velocity decay is apparent in the mixing region, where the inner flow decays by $\sim 70\%$ of its maximum outlet velocity in case 1, while that same decay is $\sim 55\%$ in all other cases. The outer flows of case 1 on the other hand experience elevated velocities relative to other cases, meaning that the outer flows in case 1 experience a milder velocity decay than other cases. It is also interesting to note that the outer flows have peaks that are shifted inwards relative to other cases, which demonstrates the quicker convergence of the flows in multi-regime mixing. The turbulence intensities shown in Figure 13 (b) are nearly identical across all cases in and after the converging region and are once again of more interest to future validation and comparison studies. It is however interesting that, unlike the velocity profiles, there are no distinctions between the turbulence intensity profile of case 1 and those of the other cases.

4.5 Flow Regime Variation Effects – 2nd Order Statistics

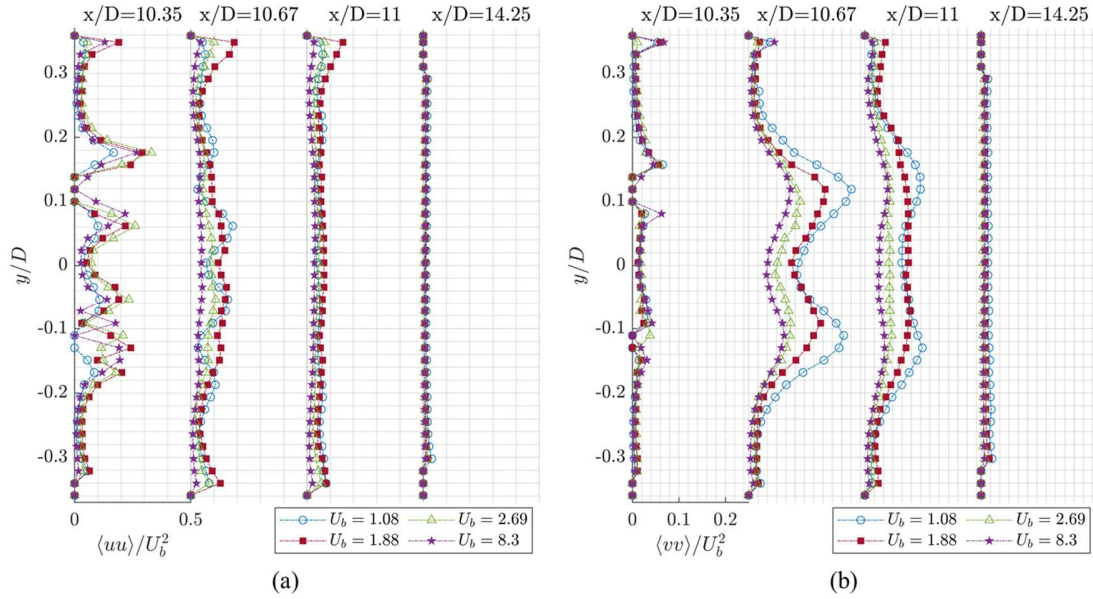


Figure 14. Spanwise profiles of $\langle uu \rangle / U_b^2$ and $\langle vv \rangle / U_b^2$ at multiple streamwise hydraulic diameters and multiple cases showing the evolution of the normal Reynolds stresses due to flow regime variation.

The $\langle uu \rangle / U_b^2$ profiles for cases 1-3 and 7, shown in Figure 14 (a), all exhibit the same behavior where peaks in the converging region corresponding to the shear layers can be seen to line up with the walls. The inner flow exhibits two shear layers on either side of the flow, and each of the outer flows exhibit one shear layer neighboring the inner flow and one boundary layer along the walls of the main channel. No significant distinction can be seen between multi-regime and turbulent mixing for $\langle uu \rangle / U_b^2$. On the other hand, the $\langle vv \rangle / U_b^2$ profiles in Figure 14 (b) show appreciable changes across all cases, particularly at $x/D = 10.67$ and 11. As mentioned earlier, the prominent peaks in the $\langle vv \rangle / U_b^2$ profiles at the mixing region are representative of mixing layers, and it is apparent that the multi-regime mixing cases (cases 1 and 2) have the most prominent peaks. The $\langle vv \rangle / U_b^2$ peaks in case 1 are approximately twice the magnitude of the peaks in case 3, while the peaks in case 2 are ~35% greater than those of case 3. This demonstrates elevated spanwise stresses in multi-regime mixing, and thereby increased spanwise motion, enabling better mixing between the flows. Figure 9 (b) demonstrates that all Reynolds stresses amongst

turbulent mixing cases are extremely similar, thereby implying that any slight differences between cases 3 and 7 in Figure 14 (b) are negligible.

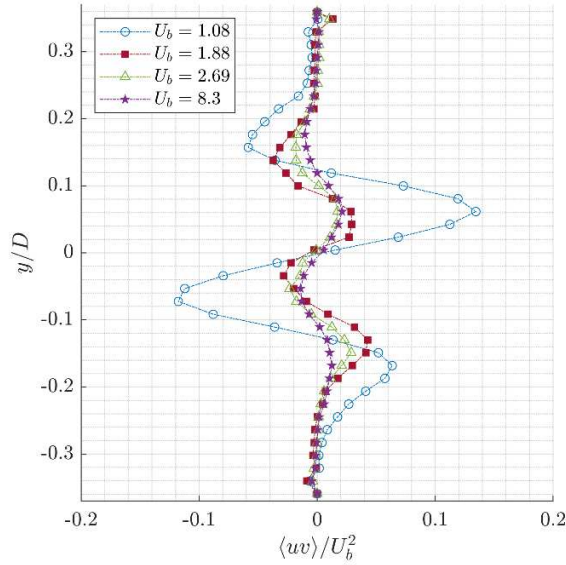


Figure 15. Spanwise profiles of $\langle uv \rangle / U_b^2$ at multiple streamwise hydraulic diameters and multiple cases showing the evolution of the shear Reynolds stresses due to flow regime variation.

The $\langle uv \rangle / U_b^2$ profiles in Figure 15 shows that multi-regime mixing exhibits elevated levels of shearing across all mixing flows. Case 1 exhibits the most elevated shearing, where its outer shear layers are ~62% more intense than those of case 3, and its inner shear layers are ~84% more intense than those of case 3. Case 2 has slightly **less** intense shearing, where its outer shear layers are ~30% more intense than those of case 3, and the inner shear layers are ~42% more intense than those of case 3. Based on the locations of the mixing layers from Figure 14 (b) and the shear layers from Figure 15, the mixing layer thicknesses span ~0.1 hydraulic diameters. This demonstrates that although multi-regime exhibits more intense shearing, the mixing layer thickness is constant throughout due to constant Re ratios.

4.6 Flow Regime Variation Effects – Velocity Decay

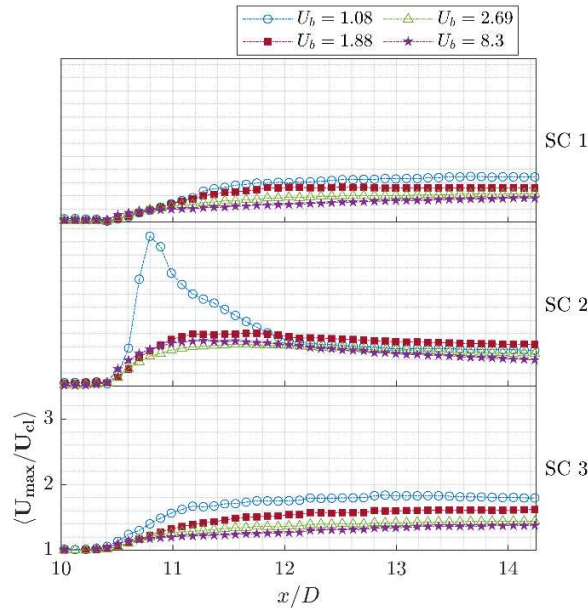


Figure 16. Streamwise decay $\langle U_{max}/U_{cl} \rangle$ of flows from cases 1-3 and 7 in each sub-channel, where SC1 corresponds to the right sub-channel, SC2 corresponds to the center sub-channel, and SC3 corresponds to the left sub-channel.

The profiles shown in Figure 16 depict the velocity decay for cases 1-3 and 7. It is clearly demonstrated that the velocity decay of the laminar inner flow of case 1 is significant relative to all other cases and anything else in literature previously discussed literature. A decay rate of ~ 6.25 is observed for the inner flow of case 1, up until the combined point at $x/D = 10.79$. The outer flows also experience elevated decay relative to the outer flows of other cases and exhibit an average decay rate of ~ 0.67 . Based on the location of the combined point and the recirculation length of 0.145, the mixing layer length can be estimated as ~ 0.3 hydraulic diameters for case 1. This demonstrates that multi-regime mixing exhibits shorter mixing layers with an intense velocity decay rate, thereby enhancing the mixing characteristics.

5. Conclusions

The Re and flow regime variation between an inner flow and two outer flows in a confined parallel flow mixing scenario was experimentally investigated via seven cases with varying Re magnitudes but constant Re ratios between the inner and outer flows. The experiment took place in the THVV MIR

tunnel, which was extensively characterized to predict the flow steady state temperature as a function of velocity, the temperature rise, the inlet velocity profiles in the transverse and spanwise directions, the inlet turbulence intensity, and the inlet flow angularity. The characterizations showed minimal variations in the flow temperatures for the experiments timespan, and strongly unidirectional inlet flows in the streamwise direction. A statistical analysis of the inlet velocimetric data revealed strong statistical convergence for 1st and 2nd order statistics.

The Re variation effects are observed by changing the Re for each of the flows prior to mixing while maintaining sufficient symmetry between the outer flows and a constant Re ratio between the inner and outer flows. All the analyses for Re variation effects from slightly turbulent flow (case 4) to highly turbulent flow (case 7) showed no major flow behavior changes other than an inverse relation between Re and recirculation lengths, and a slight variation in the decay rate. $\langle vv \rangle$ and $\langle uv \rangle$ spanwise profiles at multiple streamwise locations showed the locations of the mixing and shear layers, respectively. The distance between each inner-outer shear layer pair enabled for the determination of mixing layer thicknesses, which spanned a relatively constant 0.1 hydraulic diameters for the turbulent mixing cases (cases 4-7). The mixing layer lengths are determined by observing the peak streamwise centerline velocity decay of the inner flow, which yielded mixing lengths in the range of 0.98-0.85 hydraulic diameters for cases 4-7 respectively.

Flow regime variation between the inner and outer flows was performed in cases 1 and 2 while maintaining the constant Re ratio of the other cases. Case 1 consisted of a laminar-transitional inner-outer flow regime pair, while case 2 consisted of a transitional-turbulent pair. Analyzing flow regime variation effects revealed superior mixing characteristics with multi-regime flows, particularly in the presence of laminar flow in case 1. The laminar inner flow mixing with outer flows transitioning to turbulence yielded high decay rates with shorter mixing lengths, wherein the flows combined quicker than any other turbulent mixing cases. The decay rates of the inner flow in case 1 are nearly six times higher than those of any other turbulent mixing case (case 3-7). The outer shear layers in case 1 are ~62% more intense than

the turbulent mixing cases, and the inner shear layers are ~84% more intense. Mixing layers are found to have roughly the same thickness across all cases and are ~0.3 hydraulic diameters long in case 1 due to higher centerline velocity decay rates and quicker convergence onto the combined point.

This work communicates the benefits of multi-regime mixing through the very thorough experimental efforts with a detailed characterization of the inlet flows and multiple mixing scenarios with varying Reynolds numbers. Although literature suggests that turbulent mixing is the superior form of mixing, the results of this work illustrate that multi-regime mixing offers better characteristics including higher centerline velocity decay rates and quicker convergence of the flows onto the combined point. This work also provides detailed characterization of the experimental setup, which is very useful for validating CFD models for mixing studies. Additionally, this work demonstrates a method to achieve high levels of mixing without severe penalties in pressure drop.

The multi-regime mixing results demonstrate their superior effectiveness to turbulent mixing and can find relevance in a variety of applications. Medical applications may be able to more effectively introduce medicinal drugs or saline into a blood stream by injecting it in a turbulent regime. Chemical processes may be more effectively carried out if the streams of varying fluids or chemicals inhabited varying flow regimes prior to mixing. Even novel nuclear reactor designs can benefit from this, where TRISO fuel particles [48] may be introduced more efficiently into a liquid metal reactor [49] or a molten salt heat pipe [50] if they are carried by a laminar flow, assuming the coolant in the reactor is turbulent by design. As such, the authors encourage future and more in-depth studies of multi-regime mixing, particularly with laminar flows involved. A frequency analysis would particularly complement this work, as it can further explain the dramatic velocity decay of the inner flow, and the potential harmonic phenomena behind that decay. It could also shine a light on the recirculation pockets, and any underlying harmonics and chaotic process within them.

Acknowledgements

This work and the THVV MIR tunnel was possible using funding received from the DOE Office of Nuclear Energy's Nuclear Energy University Programs (NEUP) grant 15-8627 “Experimental Validation Data and Computational Models for Turbulent Mixing of Bypass and Coolant Jet Flows in Gas-Cooled Reactors” and from a faculty development grant from the Nuclear Regulatory Commission. This work was also supported by the Pathways to Doctorate Fellowship at Texas A&M University. The authors also wish to thank Nicholas Knight, Michael Lewandowski, Phillip Olivarez, Ryan Reed, Ihsan Shafi, and Zane Wilson and for their help in the construction of this facility and running the preliminary tests.

Declaration of Interests

The authors declare that they have no known competing financial interests or personal relationships that could have appeared to influence the work reported in this paper.

References

- 1 Choi DW, Gessner FB, Oates GC (1986) Measurements of Confined, Coaxial Jet Mixing with Pressure Gradient. *Journal of Fluids Engineering* 108:39-46.
- 2 Khayrullina A, van Hooff T, Blocken B, van Heijst GJF (2017) PIV measurements of isothermal plane turbulent impinging jets at moderate Reynolds numbers. *Experiments in Fluids* 58(31):1-16.
- 3 Bradshaw P (1971) *An Introduction to Turbulence and its Measurement*. Elsevier.
- 4 Quinn WR (2005) Measurements in the near flow field of an isosceles triangular turbulent free jet. *Experiments in Fluids* 39:111-126.
- 5 Laban A, Aleyasin SS, Tachie MF, Koupriyanov M (2019) Experimental Investigation of Nozzle Spacing Effects on Characteristics of Round Twin Free Jets. *Journal of Fluids Engineering* 141:1-11.
- 6 Oskouie RN, Tachie MF, Wang B (2020) Investigation of large-scale coherent structures and momentum interference of twin rectangular jets. *Experimental Thermal and Fluid Science* 119:1-15.
- 7 Morris EM, Aleyasin SS, Biswas N, Tachie MF (2020) Turbulent Properties of Triple Elliptic Free Jets With Various Nozzle Orientation. *Journal of Fluids Engineering* 142:1-13.
- 8 Wang T, Chintalapati S, Bunker RS, Lee CP (2000) Jet mixing in a slot. *Experimental Thermal and Fluid Science* 22(1-2):1-17.
- 9 Mehta RD (1991) Effect of velocity ratio on plane mixing layer development: Influence of the splitter plate wake. *Experiments in Fluids* 10:194-204.
- 10 Ahmed MR, Sharma SD (2000) Effect of velocity ratio on the turbulent mixing of confined, co-axial jets. *Experimental Thermal and Fluid Science* 22(1-2):19-33.
- 11 Murugan S, Huang RF, Hsu CM (2020) Flow and mixing characteristics of double-concentric jets pulsed at annular flow. *Experimental Thermal and Fluid Science* 114:1-15.
- 12 Chatzizisis YS, Coskun AU, Jonas M, Edelman ER, Feldman CL, Stone PH (2007) Role of Endothelial Shear Stress in the Natural History of Coronary Atherosclerosis and Vascular Remodeling: Molecular, Cellular, and Vascular Behavior. *Journal of the American College of Cardiology* 49(25):2379-2393.
- 13 Arasa K, Aldredge RC (2013) Computational Analysis of Catheter-Tip Geometries for Optimizing Drug Infusion in Arterial Blood Flow. *American Journal of Biomedical Engineering* 3(4):91-98.
- 14 Hassan MA, Rehme K (1981) Heat Transfer near Spacer Grids in Gas-Cooled Rod Bundles. *Nuclear Technology* 52(3):401-414.
- 15 Liu D, Gu H (2018) Study on heat transfer behavior in rod bundles with spacer grid. *International Journal of Heat and Mass Transfer* 120:1065-1075.
- 16 Clifford CE, Fradeneck AD, Oler AM, Salkhordeh S, Kimber ML (2019) Computational study of full-scale VHTR lower plenum for turbulent mixing assessment. *Annals of Nuclear Energy* 134:101-113.
- 17 Clifford CE, Kimber ML (2020) Assessment of RANS-Based Turbulence Models for Buoyancy-Influenced Forced Convection on a Heated Vertical Surface. *Journal of Verification, Validation and Uncertainty Quantification* 5:1-16.
- 18 Landfried DT, Kristo P, Clifford CE, Kimber M (2019) Design of an experimental facility with a unit cell test section for studies of the lower plenum in prismatic high temperature gas reactors. *Annals of Nuclear Energy* 133:236-247.
- 19 Bell JH, Metha RD (1988) *Contraction Design for Small Low-Speed Wind Tunnels*. National Aeronautics and Space Administration. <https://ntrs.nasa.gov/archive/nasa/casi.ntrs.nasa.gov/19880012661.pdf>. Accessed 20 July 2019.
- 20 Nedyalkov I (2012) *Design of Contraction, Test Section, Diffuser for a High-Speed Water Tunnel*. Thesis, Chalmers University of Technology.
- 21 Ripken JF (1951) *Design Study for a Closed-Jet Water Tunnel*. University of Minnesota, St. Anthony Falls Hydraulics Laboratory. https://conservancy.umn.edu/bitstream/handle/11299/107921/1/tp_009b.pdf. Accessed 19 July 2019.
- 22 Cengel YA, Cimbala JM (2006) *Fluid Mechanics Fundamentals and Applications*. McGraw Hill.
- 23 Parker Hannifin Corp (2014) *ParFab™ Design Guide*. Tech Seal Division –TSD 5420. <https://prker.co/36wVKzv>. Accessed 21 July 2019.
- 24 Reyes-Gonzalez JR (2018) *Design and Construction of a High-speed Matched Index of Refraction Facility*. Master's Thesis, Texas A&M University, <http://hdl.handle.net/1969.1/173987>.

-
- 25 Budwig RS, Westin R, "Measurement of Oil Properties", Internal Report, University of Idaho Boise, 2011.
- 26 Sabharwall P, Conder T, Skifton R, Stoots C, Kim ES (2013) PIV Uncertainty Methodologies for CFD Code Validation at the MIR Facility. INL/EXT-12-27728. <https://inldigitallibrary.inl.gov/sites/sti/sti/5901284.pdf>. Accessed 20 July 2019.
- 27 Saltelli A, Tarntola S, F. Campolongo, M. Ratto (2004) Sensitivity Analysis in Practice. John Wiley & Sons.
- 28 SimLab, Simlab Reference Manual, 2002.
- 29 Sobol LM (1990) Quasi-Monte Carlo Methods. Prog. Nucl. Energy 24: 55-61.
- 30 Sobol LM (1993) Sensitivity analysis for non linear mathematical models. Math Model Comput Exp 1: 407-414.
- 31 Weiss AG, Kristo PJ, Kimber ML (2020) Design of a Matched Index of Refraction Facility for Flow Studies with Mixing and Complex Geometries. TFEC2020:1-7.
- 32 Malitson IH (1965) Interspecimen Comparison of the Refractive Index of Fused Silica, Journal of the Optical Society of America 55:10: 1205-1209.
- 33 Durbin PA (2018) Some Recent Developments in Turbulence Closure Modeling. Annual Review of Fluid Mechanics 50:77-103.
- 34 Plesniak MW, Bell JH, Mehta RD (1993) Effects of small changes in initial conditions on mixing layer three-dimensionality. Experiments in Fluids 14:286-288.
- 35 Wieneke B (2015) PIV uncertainty quantification from correlation statistics. Measurement Science and Technology 26:1-11.
- 36 Macagno EO, Hung TK (1967) Computational and experimental study of captive annular eddy. Journal of Fluid Mechanics 28:43-64.
- 37 Guo ZY, Li DY, Liang XG (1996) Thermal effect on the recirculation zone in sudden-expansion gas flows. International Journal of Heat and Mass Transfer 39:2619-2624.
- 38 Chen L, Asai K, Nonomura T, Xi G, Liu T (2018) A review of Backward-Facing Step (BFS) flow mechanisms, heat transfer and control. Thermal Science and Engineering Progress 6:194-216.
- 39 Khan MH, Sooraj P, Sharma A, Agrawal A (2018) Flow around a cube for Reynolds numbers between 500 and 55,000. Experimental Thermal and Fluid Science 93:257-271.
- 40 Durve A, Patwardhan AW, Banerjee I, Padmakumar G, Vaidyanathan G (2012) Numerical investigation of mixing in parallel jets. Nuclear Engineering and Design 242:78-90.
- 41 Liu Y, Feng H, Olsen MG, Fox RO, Hill JC (2006) Turbulent mixing in a confined rectangular wake. Chemical Engineering Science 61:6946-6962.
- 42 Lin YF, Sheu MJ (1990) Investigation of two plane parallel turbulent jets. Experiments in Fluids 10:17-22.
- 43 Aleyasin SS, Tachie MF (2019) Statistical properties and structural analysis of three-dimensional twin round jets due to variation in Reynolds number. International Journal of Heat and Fluid Flow 76:215-230.
- 44 Nasr A, Lai JCS (1997) Two parallel plane jets: mean flow and effects of acoustic excitation. Experiments in Fluids 22:251-260.
- 45 Pope S.B. (2000) Turbulent Flows. Cambridge University Press.
- 46 Kristo PJ, Hoff CD, Craig IGR, Kimber ML (2021) Turbulent Mixing Process of a Round Jet With Slot Lobes. Journal of Fluids Engineering 143:1-13.
- 47 Mi J, Nathan GJ, Luxton RE (2000) Centerline mixing characteristics of jets from nine differently shaped nozzles. Experiments in Fluids 28:93-94.
- 48 Ali N, Al-Juwaya T, Al-Dahhan M (2017) An advanced evaluation of spouted beds scale-up for coating TRISO nuclear fuel particles using Radioactive Particle Tracking (RPT). Experimental Thermal and Fluid Science 80:90-104.
- 49 Ward B, Clark J, Bindra H (2019) Thermal stratification in liquid metal pools under influence of penetrating colder jets. Experimental Thermal and Fluid Science 103:118-125.
- 50 Xiong Y, Bo L, Qiang M, Wu Y, Zhang X, Xu P, Ma C (2017) A characteristic study on the start-up performance of molten-salt heat pipes: Experimental investigation. Experimental Thermal and Fluid Science 82:433-438.